J. Fluid Mech. (2024), *vol*. 984, R7, doi:10.1017/jfm.2024.246

Dense turbulent suspensions at a liquid interface

Seunghwan Shin[1],† **and Filippo Coletti**[1]

[1]Department of Mechanical and Process Engineering, ETH Zurich, 8092 Zurich, Switzerland

(Received 24 January 2024; revised 29 February 2024; accepted 4 March 2024)

The nexus between turbulence, particle interaction and interfacial tension is virtually unexplored, despite being highly relevant to a wealth of industrial and environmental settings. Here we investigate it by conducting experiments on non-Brownian spherical particles at the interface of turbulent liquid layers. The latter are electromagnetically stirred in a quasi-two-dimensional apparatus, while the particles are individually tracked. By systematically varying interfacial conditions, turbulence intensity, particle size and concentration from dilute to dense, we map the system behaviour over a wide parameter space. We reveal how the dynamics is governed by the balance of drag, capillarity and lubrication. Based on their scaling, we propose a phase diagram comprising three distinct regimes, characterized by widely different levels of clustering and fluctuating energy of the particles. This is quantitatively confirmed by the experimental results.

Key words: suspensions, particle/fluid flow

1. Introduction

Dense turbulent suspensions are ubiquitous in industrial and natural scenarios, from process engineering to sediment transport. However, due to the number of physical mechanisms and the daunting range of scales, reaching a predictive understanding of these systems remains a formidable and unmet challenge. Historically, research on solid–liquid mixtures has predominantly gravitated around two extrema: on one side, dense and viscous-dominated suspensions (Guazzelli, Morris & Pic 2011); on the other, turbulent and dilute ones (Balachandar & Eaton 2010). Significant progress has been made in the understanding of inertial effects in suspensions, focusing on instabilities and the onset of turbulence, e.g. in pipe flows (Matas, Morris & Guazzelli 2003; Hogendoorn & Poelma 2018; Agrawal, Choueiri & Hof 2019) and Taylor Couette flows (Majji, Banerjee & Morris 2018; Dash, Anantharaman & Poelma 2020; Morris 2020*b*). Only recently have

† Email address for correspondence: seshin@ethz.ch

researchers started bridging the gap and tackled fully turbulent dense suspensions: in experiments, through refractive-index matching and medical imaging (Zade *et al.* 2018; Baker & Coletti 2019; Alméras *et al.* 2021; Hogendoorn *et al.* 2023); and in simulations, through particle-resolved approaches (Picano, Breugem & Brandt 2015; Wang *et al.* 2016; Olivieri *et al.* 2020; Vowinckel *et al.* 2023). The nature of the measurements and the cost of the calculations, however, have imposed severe limitations on the particle material, size and number, as well as on the scales of the system. As such, the topic is still in its infancy.

An additional element, frequently encountered in solid–liquid mixtures, can further enrich the problem: the particles may be confined at fluid interface, where the dynamics is different from that in the bulk (Singh & Joseph 2005; Madivala, Fransaer & Vermant 2009; Magnaudet & Mercier 2020). The individual and collective behaviour of particles at interfaces has recently received significant attention, but the focus has been mostly on regimes where inertia is negligible or the particles are microscopic colloids (Hoekstra *et al.* 2003; Masschaele, Fransaer & Vermant 2011; Fuller & Vermant 2012; Garbin 2019). In all three classes of suspensions – dense, turbulent and interfacial – the particles tend to organize in clusters, but the underlying mechanisms are profoundly different. In dense suspensions, concentration fluctuations are driven by the hydrodynamic coupling between particles under shear (Wagner & Brady 2009; Brown & Jaeger 2014; Denn & Morris 2014). In turbulent suspensions, the particles distribute inhomogeneously when inertia prevents them from following the fluid trajectories (Bec *et al.* 2007; Balachandar & Eaton 2010; Monchaux, Bourgoin & Cartellier 2012; Brandt & Coletti 2022). At liquid interfaces, buoyancy and surface tension generate attractive forces leading to compact assemblies (Vella & Mahadevan 2005; Botto *et al.* 2012; Protière 2023). How do particles behave when these three situations intersect?

The present study focuses on the unexplored territory where turbulence, particle–particle interactions and interfacial effects are simultaneously at play. Examples of great practical relevance include microplastic pollution (van Sebille *et al.* 2020) and froth flotation in industrial processing (Quintanilla, Neethling & Brito-Parada 2021). Here we consider a seemingly simple system consisting of non-Brownian monodispersed spherical particles confined at the interface of quasi-two-dimensional (Q2D) turbulent layers. We perform extensive laboratory experiments in which turbulence intensity, interfacial tension, particle size, density and concentration are systematically varied. We investigate the propensity of the particles to form clusters and their response to the turbulent flow, both of which are shown to depend on just two non-dimensional parameters. These express the balance between the three primary forces: drag exerted by the fluid, capillarity at the interface, and lubrication between particles. We are thus able to establish a phase diagram that describes the widely different regimes exhibited by the system.

2. Methods

We employ shallow layers of conductive fluid ($CuSO_4$, 10 % aqueous solution by mass, $\rho_f = 1.08$ g ml^{-1}, $\nu = 1.0 \times 10^{-6}$ m^2 s^{-1}) in a 320 mm $\times$ 320 mm tray placed above an 8×8 array of permanent magnets, alternating their polarity in a chequerboard arrangement. Two copper electrodes immersed at opposite sides run DC current through the fluid and drive the flow by Lorentz force, the centre-to-centre distance between neighbouring magnets ($L_f = 35$ mm) being the forcing length scale. The apparatus, similar to those used in several investigations of Q2D turbulence (Kelley & Ouellette 2011; Boffetta & Ecke 2012), was fully characterized in a separate study (Shin, Coletti & Conlin 2023).

Label	ρ_p (g cm^{-3})	d_p (mm)	d_p/η	Re	ϕ	St	Bo	Θ (m^6 s^{-1})
SL	1.0	1.09 ± 0.07	0.99–2.14	566–1747	0.01–0.43	0.03–0.09	3.3×10^{-3}	2.19×10^{-16}
DL1	1.0	1.09 ± 0.07	0.57–2.10	229–1035	0.14–0.44	0.01–0.06	6.9×10^{-3}	2.05×10^{-17}
DL2	0.96	1.84 ± 0.17	0.97–3.54	192–1047	0.08–0.71	0.03–0.15	2.9×10^{-2}	3.28×10^{-16}

Table 1. Summary of the experimental parameters for this study. Other key quantities crucial for analysing trends include: the fraction of clustered particles (χ_{cl}), indicating the extent of clustering; the mean cluster diameter ($\langle D_{cl} \rangle$), defined as the weight-averaged diameter of circles that encompass each cluster; and the mean particle kinetic energy normalized by the fluid kinetic energy ($\langle E_{k,p} \rangle / \langle E_{k,f} \rangle$).

We use two arrangements of the fluid layers and two sizes of millimetric polyethylene spheres (Cospheric WPMS-1.00, CPB-0.96), as summarized in table 1. In the single-layer configuration (SL), the particles float along the surface of (though are mostly submerged in) a 7 mm-thick conductive layer (air–liquid interface). In the double-layer configurations (DL1 and DL2), a 2 mm-thick layer of mineral oil ($\rho_f = 0.84$ g ml^{-1}, $\nu = 1.9 \times 10^{-5}$ m^2 s^{-1}, Sigma Aldrich) is added on top of the 8 mm-thick conductive layer, with particles positioned at this conductive layer–oil interface (liquid–liquid interface). The double-layer configurations DL1 and DL2 employ two different particle types (table 1). To prevent surfactant contamination and maintain stable interfacial properties during measurements, each fluid layer arrangement is allowed to equilibrate overnight. Continuous agitation is ensured by the forced turbulent flow throughout the experiment, preserving consistency in fluid interface conditions. We vary the aerial fraction $\phi \equiv N_p(\pi d_p^2/4)/A_{FOV}$ between 1 % and 71 %, where N_p is the average number of particles in the field of view (FOV) of area A_{FOV}.

For each case, we analyse 100 s long videos acquired with a Phantom VEO 640 complementary metal oxide semiconductor camera operated between 100 and 240 Hz depending on the flow condition, ensuring inter-frame particle displacements around 5 pixels ($\sim$1 mm). To mitigate potential boundary effects, we image exclusively on the central region of the flow tray, ensuring that our FOV remains at least one L_f away from the sidewalls. We follow the particle centroids along Lagrangian trajectories with subpixel accuracy, using an in-house code for particle tracking velocimetry. Clusters, broadly defined as groups of adjacent particles, are detected with the DBSCAN algorithm (Ester *et al.* 1996). We set the search radius of $1.25d_p$ around each centroid to seek for a minimum of four neighbours, and verify that the results are weakly dependent on the precise value of such parameters.

We characterize each level of hydrodynamic forcing by separate experiments, in which the fluids are laden only with tracer-like polyethylene microspheres ($d_p = 75$–90 μm, Cospheric UVPMS-BG-1.00) whose motion is characterized by particle image velocimetry. Similarly to the millimetric spheres, the tracer particles also lie predominantly at the fluid interface. The root-mean-square flow velocity u_{rms} yields the Reynolds number $Re \equiv u_{rms}L_f/\nu$, where ν is the kinematic viscosity of the conductive fluid. We span a decade in Re by adjusting the DC current between 0.01 and 1.00 A. All forcing levels are in the turbulent regime (Shin *et al.* 2023) with Kolmogorov scales η comparable to d_p.

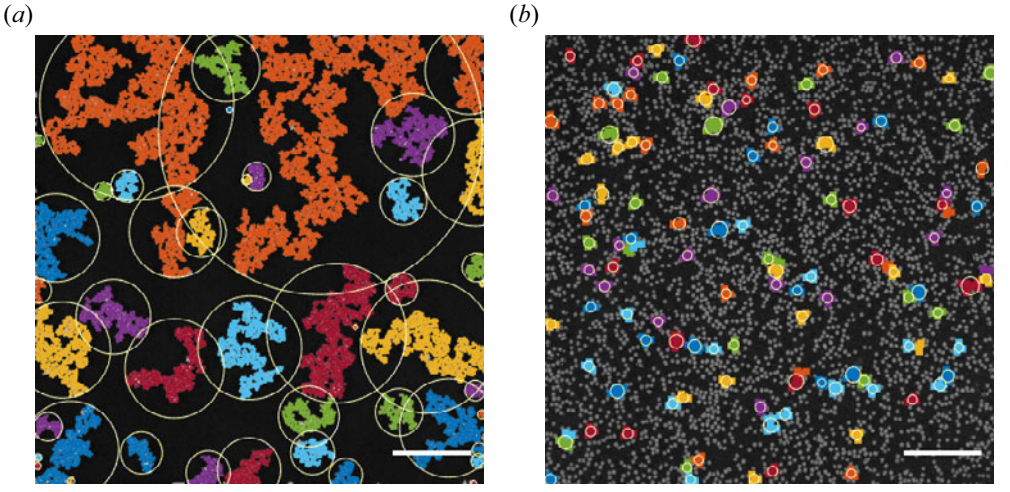

Figure 1. Example snapshots with detected clusters obtained at the same $Re = 970$ and $\phi = 0.28$ from different configurations: (*a*) SL, $\chi_{cl} = 0.99$; and (*b*) DL2, $\chi_{cl} = 0.23$. Scale bars correspond to $L_f = 35$ mm. The particles in each cluster are represented with the same colour. Circles encompassing each cluster are displayed.

3. Results and discussion

The present system shows a marked tendency to form clusters, as clear from figure 1, which displays two realizations at the same $Re = 970$ and $\phi = 0.28$, but different interfacial conditions. For comparison, we define χ_{cl} as the number of clustered particles normalized by the total number of particles. Remarkably, in the SL configuration (figure 1*a*), the fraction of clustered particles χ_{cl} is more than five times larger than in the DL2 configuration (figure 1*b*). The sizes of the clusters, approximated as the diameter D_{cl} of the circles encompassing them, also greatly differ between the two cases. To compare the dominant mechanisms at play, in the following we derive expressions for the main forces governing the particle motion: capillarity, drag and lubrication. In the considered range of parameters, electrostatic forces, e.g. due to asymmetrically distributed charges on the particles (Aveyard *et al.* 2002), are several orders of magnitude weaker.

The expression of the capillary attraction is determined by the nature of the distortion of the liquid interface around the particles. Assuming small slopes, the shape of the interface can be decomposed into Fourier modes. These expand into decaying multipoles, with each multipole excited by its corresponding Fourier mode at the contact line (Stamou, Duschl & Johannsmann 2000). When body forces and the torque on the particle are negligible, the leading-order interfacial disturbance h at a distance r from its centre is the quadrupolar distortion (Liu, Sharifi-Mood & Stebe 2018)

$$h(r) = h_{qp} d_p^2/(4r^2), \tag{3.1}$$

where h_{qp} is the mode's amplitude.

Conversely, when body forces on the particle are significant, the interfacial profile is described by the modified Bessel function of the second kind and order zero, whose asymptotic behaviour is logarithmic for small r. To first order, the vertical balance between buoyancy and interfacial tension then yields (Vella & Mahadevan 2005)

$$h(r) = \tfrac{1}{2}\Sigma d_p Bo \ln(l_c/r). \tag{3.2}$$

Here, $l_c = (\Delta\rho_f g/\gamma)^{-1/2}$ is the capillary length between fluids with density difference $\Delta\rho_f$ under the action of gravity g and interfacial tension γ; the Bond number $Bo \equiv ((\rho_f - \rho_p)gd_p^2)/4\gamma$, with ρ_f the density of the fluid on which the particle of density ρ_p is floating; and

$$\Sigma \equiv \tfrac{1}{3}(2\rho_f/\rho_p - 1) - \tfrac{1}{2}\cos\theta + \tfrac{1}{6}\cos^3\theta \tag{3.3}$$

is a dimensionless buoyancy-subtracted weight of the particle with the contact angle θ.

In all the considered configurations, $Bo \ll 1$ (table 1), which indicates that the distortion induced by body forces is negligibly small. For example, for a particle in the SL configuration, where it is predominantly immersed ($\theta < \pi/2$), such distortion at the contact-line radius would be $<1\,\mu$m, much smaller than the quadrupolar distortion of $\sim 14\,\mu$m. Thus, while the slower-decaying contribution from body forces becomes significant at large separations, the quadrupolar contribution remains dominant for the groups of adjacent particles considered here. Therefore, we write (Stamou *et al.* 2000; Liu *et al.* 2018)

$$F_{capillary} = -3\pi\gamma h_{qp}^2 d_p^4/r^5, \tag{3.4}$$

with r the centre-to-centre interparticle distance.

Rather than characterizing h_{qp} (which requires precise measurements of the contact angles), we perform separate experiments in which particle pairs are placed in the fluid layer configurations and approach each other due to capillary attraction. In this creeping flow regime, $F_{capillary} = -F_{drag} = -(3/2)\pi\mu\dot{r}d_p$, where $\dot{r}/2$ is the velocity of each particle in the pair and μ is the dynamic viscosity of the conductive fluid in which the particles are mostly submerged. This leads to the power-law relation (Loudet *et al.* 2005; Liu *et al.* 2018)

$$r_0^6 - r^6(t) = \Theta t, \tag{3.5}$$

where r_0 is the initial interparticle distance at time $t = 0$ and $\Theta = 12\gamma h_{qp}^2 d_p^3/\mu$. We experimentally verify this relation by tracking particle pairs; see figure 2. The excellent agreement with (3.5) suggests that the interface deformation causes only marginal deviations from the Stokesian solution (Loudet *et al.* 2020). Least-squares fits to (3.5) yield values of Θ, and thus h_{qp}, which are utilized for evaluating the capillary attraction in (3.4).

When the fluid flow is turbulent, the drag pulling a pair of particles away from each other is

$$F_{drag} = 3\pi\mu d_p \Delta u_f, \tag{3.6}$$

where Δu_f is the velocity difference between two fluid locations corresponding to a pair of closely situated particles, evaluated along the separation vector between the pair. As we are interested in the interaction of adjacent particles, we approximate $\Delta u_f \sim d_p\dot{\epsilon}_{max}$, where $\dot{\epsilon}_{max}$ is the maximum principal strain rate. The Stokesian assumption is justified by the particle Reynolds number $Re_p = d_p\Delta u_f/\nu$ being relatively small. Indeed, as the density of the particles approximately matches that of the fluid, Re_p is equivalent (within a geometric factor) to the Stokes number $St \equiv \tau_p u_{rms}/L_f$ (Ouellette, O'Malley & Gollub 2008), which is listed in table 1. The particle response time is taken as $\tau_p = \rho_p d_p^2/(18\mu)$, neglecting finite-$Re_p$ corrections. In turn, the values of St indicate that the particles have insignificant inertia with respect to the energetic scales of the flow.

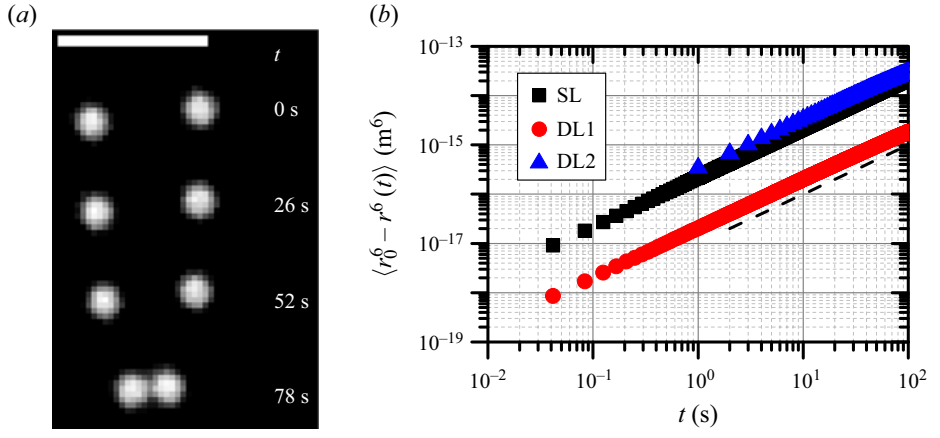

Figure 2. (*a*) A time series of a pair of particles in DL1 configuration. The scale bar indicates 5 mm. (*b*) Plot of $\langle r_0^6 - r^6\rangle$ versus t in the three configurations. The dashed line indicates $\sim t$ scaling relation.

The strain rate is estimated by schematizing the flow field as an array of Taylor–Green vortices, whose velocity components in directions x and y are, respectively,

$$\left.\begin{aligned} u &= U\cos\frac{\pi x}{L_f}\sin\frac{\pi y}{L_f},\\ v &= -U\sin\frac{\pi x}{L_f}\cos\frac{\pi y}{L_f}, \end{aligned}\right\} \tag{3.7}$$

for which $\dot{\epsilon}_{max} \approx (\pi/\sqrt{2})(u_{rms}/L_f)$. While simplified, such a representation of the flow yields excellent quantitative agreement with the statistical properties of 2D turbulence (Shin *et al.* 2023). It follows that

$$F_{drag} = \left(\frac{3\pi^2}{\sqrt{2}}\right)\frac{\mu d_p^2 u_{rms}}{L_f}. \tag{3.8}$$

We then define the capillary number given by the ratio of F_{drag} and $F_{capillary}$ evaluated for $r = d_p$:

$$Ca = \frac{6\sqrt{2}\pi d_p^6 u_{rms}}{\Theta L_f}. \tag{3.9}$$

In figures 1(*a*) and 1(*b*), $Ca = 0.16$ and 2.49, respectively, which accounts for the much stronger clustering in the former: drag from the straining flow dominates, and clusters are disrupted for $Ca \gg 1$, and *vice versa* for $Ca \ll 1$. This is confirmed in figure 3(*a*), showing χ_{cl} versus Ca: collectively, the data adhere to a unified trend, confirming the role of Ca as the controlling parameter. This applies at aerial fractions $\phi \leq 0.20$, for which F_{drag} and $F_{capillary}$ are the main forces.

For large ϕ, on the other hand, we observe stronger clustering and a reduction in the root-mean-square particle velocity, which we attribute to additional viscous dissipation by the lubrication force (Wagner & Brady 2009; Morris 2020*a*). For a pair of nearby particles

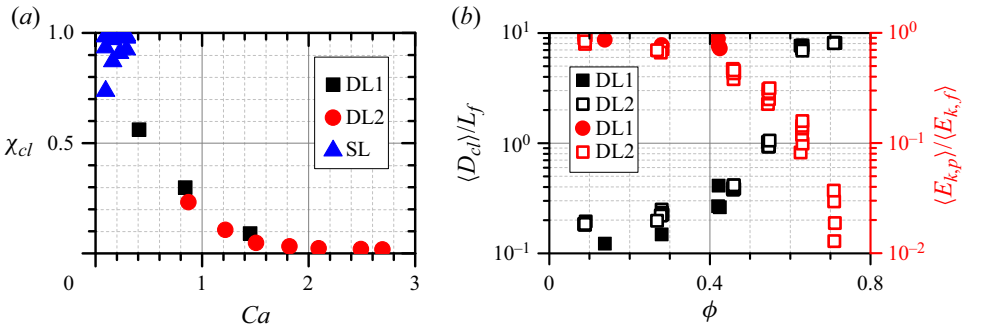

Figure 3. (*a*) The fraction of clustered particles (χ_{cl}) versus Ca at $\phi < 0.20$. (*b*) The normalized mean cluster diameter ($\langle D_{cl}\rangle/L_f$, black) and the normalized particle kinetic energy ($\langle E_{k,p}\rangle/\langle E_{k,f}\rangle$, red) as functions of ϕ at $Ca > 1$.

moving at relative speed Δu_p, this is

$$F_{lubrication} = \frac{3\pi\mu d_p^2 \Delta u_p}{8(r - d_p)}. \tag{3.10}$$

Relating $\Delta u_p \approx r\dot{\epsilon}_{max} \approx r(\pi/\sqrt{2})(u_{rms}/L_f)$, we approximate

$$F_{lubrication} = \frac{3\pi^2\mu d_p^2 u_{rms} r}{8\sqrt{2}(r - d_p)L_f}. \tag{3.11}$$

Balancing $F_{lubrication}$ and F_{drag} yields the separation $r/d_p = 9/8$: lubrication prevails when neighbouring particles are, on average, closer than such distance, dissipating their kinetic energy. To obtain the corresponding aerial fraction, we employ random sequential adsorption (Evans 1993) to distribute in 2D space non-overlapping circles with a range of diameters comparable to those of our particles, i.e. assuming a normal distribution of diameters with the same standard deviations as in table 1. This synthetic method indicates that the average nearest-neighbour separation reaches $(9/8)d_p$, for $\phi \sim 0.4$. This approximate threshold is confirmed in figure 3(*b*), showing the mean cluster diameter $\langle D_{cl}\rangle$ normalized by the forcing length scale L_f, and the particle kinetic energy $\langle E_{k,p}\rangle$ normalized by the fluid kinetic energy $\langle E_{k,f}\rangle$ (measured in the unladen case under the same forcing). For cases in which drag overcomes capillarity ($Ca > 1$), the trends for different interfacial conditions are quantitatively similar: for $\phi > 0.4$, $\langle D_{cl}\rangle$ grows rapidly and $\langle E_{k,p}\rangle/\langle E_{k,f}\rangle$ dips. The cluster size appears to plateau at $\sim 8.5L_f$, corresponding to the diagonal of the square FOV of size $6L_f$, i.e. the maximum size detectable by the imaging system. That is, above approximately $\phi = 0.6$, the system percolates forming a macrocluster of vanishing small kinetic energy that spans the entire domain.

In summary, our analysis suggests three distinct regimes depending on the balance of three factors: capillarity, viscous drag and lubrication. When $Ca < 1$, capillary attraction holds particles together and leads to the formation of tightly bound clusters. When $Ca > 1$, the strain field of the fluid acts on the particles through viscous drag and breaks up the clusters, as long as $\phi < 0.4$; while lubrication preserves slowly moving clusters at higher concentrations. This is schematically illustrated in the phase diagram in figure 4(*a*) and by the snapshots in figure 4(*b*) corresponding to the three regimes: capillary-driven clustering, drag-driven break-up and lubrication-driven clustering. We remark that the identified values of the control parameters Ca and ϕ are not expected to be critical

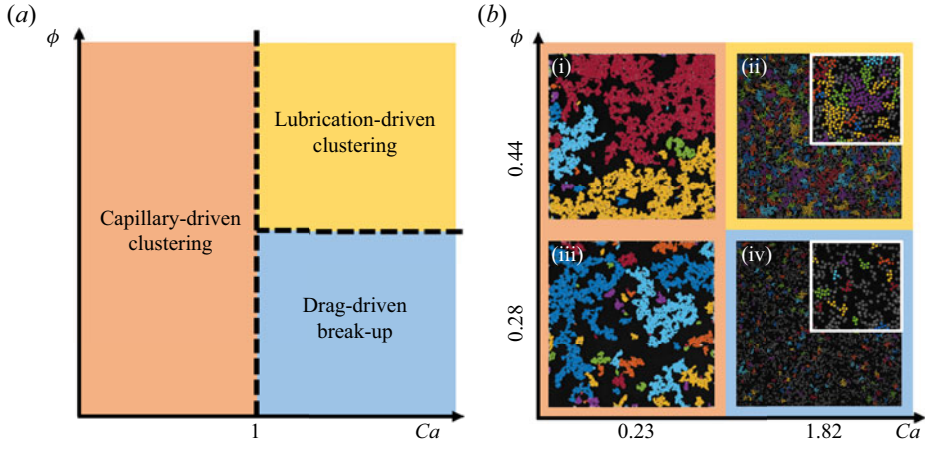

Figure 4. (*a*) Three predicted clustering/break-up regimes in Ca–ϕ space. (*b*) Snapshots from different configurations, illustrating varying degrees of clustering with χ_{cl} values of 0.991 and 0.624 (i), (ii), and 0.990 and 0.249 (iii), (iv). Insets provide magnified views to highlight differences. Particles within each cluster are represented with the same colour.

thresholds, as the considered process does not entail abrupt transitions. In fact, within each one of these regimes, quantitative changes are still observed as the control parameters are varied. For example, in the capillary-driven clustering regime, the aggregates grow bigger with increasing ϕ, as more particles stick to larger groups and these merge together; this is evident by comparing the two snapshots at $Ca = 0.23$ in figure 4(*b*). However, those differences appear quantitative rather than qualitative, and the main mechanisms responsible for the behaviour in each regime are not altered.

The proposed phase diagram is supported by the contour maps over the Ca–ϕ space displayed in figure 5, which depicts the behaviour of the key observables discussed above for the parameter space we explored. In particular, in the map of χ_{cl} (figure 5*a*), dense vertical contour lines at $Ca < 1$ give way to horizontal ones at $Ca > 1$, bounding the drag-driven break-up regime. The trend of the normalized mean cluster size $\langle D_{cl}\rangle/L_f$ (figure 5*b*) is similar, with a sharp increase for $\phi \geq 0.4$. Over this range of concentrations, larger clusters are often centred at the core of vortical structures, where the local strain rate is insufficient to tear them apart (see the supplementary movies available at https://doi.org/10.1017/jfm.2024.246). Furthermore, comparing this map with that of the particle kinetic energy $\langle E_{k,p}\rangle/\langle E_{k,f}\rangle$, we notice that the motion of clustered particles is greatly inhibited when $\langle D_{cl}\rangle$ becomes much larger than L_f, which is the typical size of the forced turbulent eddies (Boffetta & Ecke 2012; Shin *et al.* 2023): as a cluster spans multiple counter-rotating eddies, the latter are not effective in moving it around. Lastly, the energy maps reveal that even giant clusters spanning the entire domain (e.g. at $\phi \geq 0.6$) have different dynamics depending on Ca: they are effectively rigid and static when capillarity dominates ($Ca < 1$), while they are softer and dynamic when drag takes over ($Ca > 1$); see the supplementary movies.

We remark that the fluid kinetic energy is not directly measured, as the millimetre-sized particles impede sufficient optical access. The values we use, evaluated at the same forcing and $\phi = 0$, are, however, expected to be a close approximation of the fluid energy in the suspensions. The submerged particles only occupy a minor portion of the conductive fluid layer and therefore do not significantly alter the Lorentz force. The frictional dissipation on the particle surfaces is also a fraction of that experienced by the fluid on the floor of

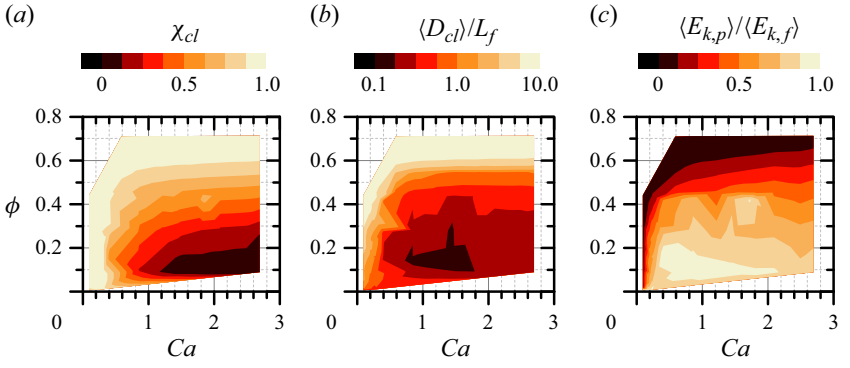

Figure 5. Phase diagram in Ca–ϕ space to characterize the particle behaviour, mapping (*a*) χ_{cl}, (*b*) $\langle D_{cl}\rangle/L_f$ and (*c*) $\langle E_{k,p}\rangle/\langle E_{k,f}\rangle$.

the tray, which dominates the dissipation rate (Shin *et al.* 2023), except when giant rigid clusters of vanishing kinetic energy are formed.

4. Conclusion

We have investigated the spatial distribution and motion of particles at the interface of Q2D turbulent liquid layers. Those are governed by the balance of capillarity, drag and lubrication, and two non-dimensional parameters rule the system: the capillarity number Ca and the aerial fraction ϕ (equivalently, the normalized interparticle distance r/d_p). When $Ca < 1$, capillary attraction effectively binds particles into tight clusters. When $Ca > 1$, drag from the straining fluid flow prevents the formation of large clusters as long as $\phi < 0.4$; while short-range lubrication yields slow-moving clusters when $\phi > 0.4$. The present analysis assumes that the governing forces are independent, while coupling is expected, e.g. as capillary-driven clustering causes changes in the effective drag force. The agreement between prediction and observation, however, indicates that such a simplification is appropriate to first order.

This study opens several avenues for future investigations in related regimes. Clearly, the proposed phase diagram and its boundaries depend on the chosen configurations and the validity of the assumptions we made. For example, marine plastics include millimetre-sized particles but also micrometre-sized particles (van Sebille *et al.* 2020), and the latter may hardly aggregate into cohesive clusters of size comparable to the energetic eddies. On the other hand, for larger Bo (e.g. particles only partially submerged in free-surface flows), the monopole contribution dominates and the capillary attraction decays much more slowly, with $F_{capillary} \sim r^{-1}$ (Vella & Mahadevan 2005), with significant implications for the prevalence of clustering. Under conditions of more intense turbulence close to the surface, large surface deformations may occur, influencing the transport of floating particles. Moreover, Q2D turbulence has peculiar characteristics which separate it from its classic three-dimensional (3D) counterpart, notably an inverse cascade of energy towards the larger scales (Tabeling 2002; Boffetta & Ecke 2012). Still, it possesses essential hallmarks including chaotic/nonlinear behaviour, rotationality, stretching, folding and mixing of fluid elements, and wide ranges of spatio-temporal scales, making it a valuable system to investigate fundamental turbulence dynamics (Suri *et al.* 2017; Ballouz & Ouellette 2020), particularly in the context of particle suspensions (Boffetta, De Lillo & Gamba 2004; Goto & Vassilicos 2008; Ouellette *et al.* 2008).

An important aspect of 3D interfacial flows is the non-solenoidal nature of the velocity field along the surface, which is known to play a significant role for colloids in viscous flows (Samaniuk & Vermant 2014; Pourali *et al.* 2021). Further research is warranted to explore this effect in dense suspensions of particles floating on the surface of a turbulent body of water. Overall, we expect that the important mechanisms and trends revealed by the considered configurations will extend beyond the present model problem, including regimes where additional forces, such as electrostatics (van Baalen, Vialetto & Isa 2023) and soft granular repulsion (Gupta *et al.* 2022), become significant. Finally, the present findings can also be relevant to systems in which the multi-scale, turbulent-like behaviour is rooted in the interaction and collective dynamics of active elements, such as bacteria (Dunkel *et al.* 2013; Peng, Liu & Cheng 2021) and self-propelled particles (Bourgoin *et al.* 2020).

Supplementary movies. Supplementary movies are available at https://doi.org/10.1017/jfm.2024.246.

Acknowledgements. We thank L. Botto, J. Vermant and L. Isa for fruitful discussions.

Funding. This work was supported by the Swiss National Science Foundation, grant number 200021-207318.

Declaration of interests. The authors report no conflict of interest.

Author ORCIDs.
Seunghwan Shin https://orcid.org/0000-0001-6581-1523;
Filippo Coletti https://orcid.org/0000-0001-5344-2476.

References

Agrawal, N., Choueiri, G.H. & Hof, B. 2019 Transition to turbulence in particle laden flows. *Phys. Rev. Lett.* **122** (11), 114502.

Alméras, E., Risso, F., Masbernat, O. & Fox, R.O. 2021 Statistics of velocity fluctuations in a homogeneous liquid fluidized bed. *Phys. Rev. Fluids* **6** (3), 034301.

Aveyard, R., *et al.* 2002 Measurement of long-range repulsive forces between charged particles at an oil–water interface. *Phys. Rev. Lett.* **88** (24), 246102.

van Baalen, C., Vialetto, J. & Isa, L. 2023 Tuning electrostatic interactions of colloidal particles at oil–water interfaces with organic salts. *Phys. Rev. Lett.* **131**, 128202.

Baker, L.J. & Coletti, F. 2019 Experimental study of negatively buoyant finite-size particles in a turbulent boundary layer up to dense regimes. *J. Fluid Mech.* **866**, 598–629.

Balachandar, S. & Eaton, J.K. 2010 Turbulent dispersed multiphase flow. *Annu. Rev. Fluid Mech.* **42**, 111–133.

Ballouz, J.G. & Ouellette, N.T. 2020 Geometric constraints on energy transfer in the turbulent cascade. *Phys. Rev. Fluids* **5** (3), 034603.

Bec, J., Biferale, L., Cencini, M., Lanotte, A., Musacchio, S. & Toschi, F. 2007 Heavy particle concentration in turbulence at dissipative and inertial scales. *Phys. Rev. Lett.* **98** (8), 084502.

Boffetta, G., De Lillo, F. & Gamba, A. 2004 Large scale inhomogeneity of inertial particles in turbulent flows. *Phys. Fluids* **16** (4), L20–L23.

Boffetta, G. & Ecke, R.E. 2012 Two-dimensional turbulence. *Annu. Rev. Fluid Mech.* **44**, 427–482.

Botto, L., Lewandowski, E.P., Cavallaro, M. & Stebe, K.J. 2012 Capillary interactions between anisotropic particles. *Soft Matt.* **8** (39), 9957–9971.

Bourgoin, M., *et al.* 2020 Kolmogorovian active turbulence of a sparse assembly of interacting Marangoni surfers. *Phys. Rev.* X **10** (2), 021065.

Brandt, L. & Coletti, F. 2022 Particle-laden turbulence: progress and perspectives. *Annu. Rev. Fluid Mech.* **54**, 159–189.

Brown, E. & Jaeger, H.M. 2014 Shear thickening in concentrated suspensions: phenomenology, mechanisms and relations to jamming. *Rep. Prog. Phys.* **77** (4), 046602.

Dash, A., Anantharaman, A. & Poelma, C. 2020 Particle-laden Taylor–Couette flows: higher-order transitions and evidence for azimuthally localized wavy vortices. *J. Fluid Mech.* **903**, A20.

DENN, M.M. & MORRIS, J.F. 2014 Rheology of non-Brownian suspensions. *Annu. Rev. Chem. Biomol. Engng* **5**, 203–228.

DUNKEL, J., *et al.* 2013 Fluid dynamics of bacterial turbulence. *Phys. Rev. Lett.* **110** (22), 228102.

ESTER, M., KRIEGEL, H.P., SANDER, J. & XU, X. 1996 A density-based algorithm for discovering clusters in large spatial databases with noise. In *KDD'96 Proc. Second Int. Conf. Knowl. Discov. Data Mining*, pp. 226–231. AAAI.

EVANS, J.W. 1993 Random and cooperative sequential adsorption. *Rev. Mod. Phys.* **65** (4), 1281.

FULLER, G.G. & VERMANT, J. 2012 Complex fluid–fluid interfaces: rheology and structure. *Annu. Rev. Chem. Biomol. Engng* **3**, 519–543.

GARBIN, V. 2019 Collapse mechanisms and extreme deformation of particle-laden interfaces. *Curr. Opin. Colloid Interface Sci.* **39**, 202–211.

GOTO, S. & VASSILICOS, J.C. 2008 Sweep-stick mechanism of heavy particle clustering in fluid turbulence. *Phys. Rev. Lett.* **100** (5), 054503.

GUAZZELLI, E., MORRIS, J.F. & PIC, S. 2011 *A Physical Introduction to Suspension Dynamics*. Cambridge University Press.

GUPTA, M., CHAUDHURI, P., BEC, J. & RAY, S.S. 2022 Turbulent route to two-dimensional soft crystals. *Phys. Rev.* E **106** (6), L062601.

HOEKSTRA, H., VERMANT, J., MEWIS, J. & FULLER, G.G. 2003 Flow-induced anisotropy and reversible aggregation in two-dimensional suspensions. *Langmuir* **19** (22), 9134–9141.

HOGENDOORN, W., BREUGEM, W.-P., FRANK, D., BRUSCHEWSKI, M., GRUNDMANN, S. & POELMA, C. 2023 From nearly homogeneous to core-peaking suspensions: insight in suspension pipe flows using MRI and DNS. *Phys. Rev. Fluids* **8** (12), 124302.

HOGENDOORN, W. & POELMA, C. 2018 Particle-laden pipe flows at high volume fractions show transition without puffs. *Phys. Rev. Lett.* **121** (19), 194501.

KELLEY, D.H. & OUELLETTE, N.T. 2011 Separating stretching from folding in fluid mixing. *Nat. Phys.* **7** (6), 477.

LIU, I.B., SHARIFI-MOOD, N. & STEBE, K.J. 2018 Capillary assembly of colloids: interactions on planar and curved interfaces. *Annu. Rev. Condens. Matt. Phys.* **9**, 283–304.

LOUDET, J.C., ALSAYED, A.M., ZHANG, J. & YODH, A.G. 2005 Capillary interactions between anisotropic colloidal particles. *Phys. Rev. Lett.* **94** (1), 018301.

LOUDET, J.C., QIU, M., HEMAUER, J. & FENG, J.J. 2020 Drag force on a particle straddling a fluid interface: influence of interfacial deformations. *Eur. Phys. J.* E **43**, 1–13.

MADIVALA, B., FRANSAER, J. & VERMANT, J. 2009 Self-assembly and rheology of ellipsoidal particles at interfaces. *Langmuir* **25** (5), 2718–2728.

MAGNAUDET, J. & MERCIER, M.J. 2020 Particles, drops, and bubbles moving across sharp interfaces and stratified layers. *Annu. Rev. Fluid Mech.* **52**, 61–91.

MAJJI, M.V., BANERJEE, S. & MORRIS, J.F. 2018 Inertial flow transitions of a suspension in Taylor–Couette geometry. *J. Fluid Mech.* **835**, 936–969.

MASSCHAELE, K., FRANSAER, J. & VERMANT, J. 2011 Flow-induced structure in colloidal gels: direct visualization of model 2D suspensions. *Soft Matt.* **7** (17), 7717–7726.

MATAS, J.-P., MORRIS, J.F. & GUAZZELLI, E. 2003 Transition to turbulence in particulate pipe flow. *Phys. Rev. Lett.* **90** (1), 014501.

MONCHAUX, R., BOURGOIN, M. & CARTELLIER, A. 2012 Analyzing preferential concentration and clustering of inertial particles in turbulence. *Intl J. Multiphase Flow* **40**, 1–18.

MORRIS, J.F. 2020*a* Shear thickening of concentrated suspensions: recent developments and relation to other phenomena. *Annu. Rev. Fluid Mech.* **52**, 121–144.

MORRIS, J.F. 2020*b* Toward a fluid mechanics of suspensions. *Phys. Rev. Fluids* **5** (11), 110519.

OLIVIERI, S., BRANDT, L., ROSTI, M.E. & MAZZINO, A. 2020 Dispersed fibers change the classical energy budget of turbulence via nonlocal transfer. *Phys. Rev. Lett.* **125** (11), 114501.

OUELLETTE, N.T., O'MALLEY, P.J.J. & GOLLUB, J.P. 2008 Transport of finite-sized particles in chaotic flow. *Phys. Rev. Lett.* **101** (17), 174504.

PENG, Y., LIU, Z. & CHENG, X. 2021 Imaging the emergence of bacterial turbulence: phase diagram and transition kinetics. *Sci. Adv.* **7** (17), eabd1240.

PICANO, F., BREUGEM, W.-P. & BRANDT, L. 2015 Turbulent channel flow of dense suspensions of neutrally buoyant spheres. *J. Fluid Mech.* **764**, 463–487.

POURALI, M., *et al.* 2021 Drag on a spherical particle at the air–liquid interface: interplay between compressibility, Marangoni flow, and surface viscosities. *Phys. Fluids* **33** (6), 062103.

PROTIÈRE, S. 2023 Particle rafts and armored droplets. *Annu. Rev. Fluid Mech.* **55**, 459–480.

QUINTANILLA, P., NEETHLING, S.J. & BRITO-PARADA, P.R. 2021 Modelling for froth flotation control: a review. *Miner. Engng* **162**, 106718.

SAMANIUK, J.R. & VERMANT, J. 2014 Micro and macrorheology at fluid–fluid interfaces. *Soft Matt.* **10** (36), 7023–7033.

VAN SEBILLE, E., *et al.* 2020 The physical oceanography of the transport of floating marine debris. *Environ. Res. Lett.* **15** (2), 023003.

SHIN, S., COLETTI, F. & CONLIN, N. 2023 Transition to fully developed turbulence in quasi-two-dimensional electromagnetic layers. *Phys. Rev. Fluids* **8** (9), 094601.

SINGH, P. & JOSEPH, D.D. 2005 Fluid dynamics of floating particles. *J. Fluid Mech.* **530**, 31–80.

STAMOU, D., DUSCHL, C. & JOHANNSMANN, D. 2000 Long-range attraction between colloidal spheres at the air–water interface: the consequence of an irregular meniscus. *Phys. Rev.* E **62** (4), 5263–5266.

SURI, B., TITHOF, J., GRIGORIEV, R.O. & SCHATZ, M.F. 2017 Forecasting fluid flows using the geometry of turbulence. *Phys. Rev. Lett.* **118** (11), 114501.

TABELING, P. 2002 Two-dimensional turbulence: a physicist approach. *Phys. Rep.* **362** (1), 1–62.

VELLA, D. & MAHADEVAN, L. 2005 The "Cheerios effect". *Am. J. Phys.* **73** (9), 817–825.

VOWINCKEL, B., ZHAO, K., ZHU, R. & MEIBURG, E. 2023 Investigating cohesive sediment dynamics in open waters via grain-resolved simulations. *Flow* **3**, E24.

WAGNER, N.J. & BRADY, J.F. 2009 Shear thickening in colloidal dispersions. *Phys. Today* **62** (10), 27–32.

WANG, L.-P., PENG, C., GUO, Z. & YU, Z. 2016 Lattice Boltzmann simulation of particle-laden turbulent channel flow. *Comput. Fluids* **124**, 226–236.

ZADE, S., COSTA, P., FORNARI, W., LUNDELL, F. & BRANDT, L. 2018 Experimental investigation of turbulent suspensions of spherical particles in a square duct. *J. Fluid Mech.* **857**, 748–783.